Additive Manufacturing 59 (2022) 103120

Contents lists available at ScienceDirect

Additive Manufacturing

journal homepage: www.elsevier.com/locate/addma

Additively manufactured Haynes-282 monoliths containing thin wall struts of varying thicknesses

Bryan Lim [a,b,*], Hansheng Chen [a,b], Keita Nomoto [a,b], Zibin Chen [c], Alec I. Saville [d], Sven Vogel [e], Amy J. Clarke [d], Anna Paradowska [f,g], Mark Reid [g], Sophie Primig [h], Xiaozhou Liao [a,b], Sudarsanam Suresh Babu [i,j], Andrew J. Breen [a,b], Simon P. Ringer [a,b,*]

[a] *School of Aerospace, Mechanical & Mechatronic Engineering, The University of Sydney, Sydney, NSW, Australia*
[b] *Australian Centre for Microscopy & Microanalysis, The University of Sydney, Sydney, NSW, Australia*
[c] *Department of Industrial and Systems Engineering, The Hong Kong Polytechnic University, Kowloon, Hong Kong*
[d] *Department of Metallurgical and Materials Engineering, Colorado School of Mines, Golden, CO, USA*
[e] *Materials Science and Technology Division, Los Alamos National Laboratory, Los Alamos, NM, USA*
[f] *School of Civil Engineering, The University of Sydney, Sydney, NSW, Australia*
[g] *Australian Nuclear Science and Technology Organisation, Lucas Heights, NSW, Australia*
[h] *School of Materials Science and Engineering, UNSW Sydney, Sydney, NSW, Australia*
[i] *Department of Mechanical, Aerospace, and Biomedical Engineering, University of Tennessee, Knoxville, TN, USA*
[j] *Manufacturing Demonstration Facility, Manufacturing Sciences Division, Oak Ridge National Lab, Knoxville, TN, USA*

ARTICLE INFO

Keywords:
Hardness
Residual stress
Neutron diffraction
Superalloy
Electron beam powder bed fusion

ABSTRACT

Magnitude and distribution of residual stresses in additively manufactured Ni-based superalloys may impact the mechanical performance of as-fabricated parts. Though electron beam powder bed fusion (E-PBF) can produce components with minimal defects and residual stresses compared to laser powder bed fusion and directed energy deposition, variations of them may occur within the complex geometry of a component, due to inherent variations of thermal signatures and the evolution of section modulus along the build direction. This work reveals the residual stress distribution, characterised from neutron diffraction, of an as-fabricated Haynes 282 monolith containing internal cube voids and thin wall struts of varying thicknesses. Complementary local hardness measurements and multi-scale microscopy were used to investigate the geometry-structure-property relationships. Observed variations in hardness were attributed to a combination of type I macro-scale residual stresses and variations in bimodal γ' precipitation behaviour. The results highlight the influence of residual stresses and microstructure on the mechanical properties of E-PBF Haynes 282.

1. Introduction

Haynes 282 (H282) is a current generation Ni-based superalloy, developed and adopted for hot section parts in gas turbines for aircraft and power generation [1,2]. It is considered one of the forerunning candidates for turbine components in new, advanced ultrasupercritical power plant applications [3,4]. These powerplants aim for net plant efficiencies of ~47%, up from current-generation powerplant designs of 37% efficiency [5], attained through steam operating temperatures and pressures up to 760 °C and 31 MPa, respectively. This increase in thermal efficiency was estimated to reduce CO_2 and fuel-related emissions from 0.85 to 0.67 tonnes/MWh, a significant ~21% reduction [5].

H282's high-temperature strength is achieved primarily through intermetallic $L1_2$ γ' precipitation. However, compared to other common Ni-based superalloys such as Waspaloy and Rene-41, fully aged H282 has a comparably lower γ' phase fraction of 19%, whilst retaining equivalent tensile and creep properties [2,6]. This severely reduces the strain-age cracking tendency – greatly increasing its fabricability and weldability compared to other superalloys [6]. Furthermore, long term thermal exposure at 760 °C shows increased room temperature yield strength, without the formation of topologically close packed (TCP) phases. It is noteworthy that the TCP phases are brittle and deleterious and often found in other Ni-based superalloys such as Rene-41 [1]. With the design and development of new generation of steam and gas turbines

---

[*] Corresponding authors at: School of Aerospace, Mechanical & Mechatronic Engineering, The University of Sydney, Sydney, NSW, Australia.
E-mail addresses: bryan.lim@sydney.edu.au (B. Lim), simon.ringer@sydney.edu.au (S.P. Ringer).

https://doi.org/10.1016/j.addma.2022.103120
Received 27 June 2022; Received in revised form 28 August 2022; Accepted 30 August 2022

for higher thermal efficiencies, the inevitability of complex geometries for sub-components poses challenges to traditional casting processes in terms of yield and cost [7].

Based on the above needs, there is an impetus to fabricate H282 complex geometrical components through additive manufacturing (AM). Recent publications have reported successful processing of H282 via various AM technologies, such as directed energy deposition by laser (DED-L) [8], laser powder bed fusion (L-PBF) [9,10], and electron beam powder bed fusion (E-PBF) [11]. Electron beam powder bed fusion (E-PBF) is a particularly promising method to produce AM H282 containing in-situ γ' precipitation with relatively lower residual stresses and reduced cracking tendency [12]. Dependant on fabrication parameters, L-PBF has been shown to be capable of imparting over 300% more residual stresses compared to E-PBF of the same alloy system, which had negligible residual stresses [13]. As E-PBF occurs in vacuum and at elevated bed temperatures (typically ~1000 °C for Ni-based superalloys) [12,14], this leads to reduced thermal gradients within the bulk of the AM builds, allowing for intrinsic heat treatment opportunities during processing or cooling (and perhaps complex thermal cycling) from the processing temperature [15,16]. If the pre-heat temperature is above the solvus temperature, precipitation will occur during the final cooling stage. If the preheat temperature is below the solvus temperature, a build may undergo 'aging' and initiate γ' precipitation. E-PBF uses an electron beam source and scanning strategies to preheat and sinter, which is followed by melting at specific locations. After solidification of these molten regions, the built part is lowered and succeeding [i.e., $(n+1)^{th}$] layers of powder are raked over the previous layer (i.e. nth layer), repeating the process. One key factor in this process flow for a complex geometry is that each and every layer may contain differing cross sections, based upon the orientation and nesting of this geometry within the overall build. Therefore, we hypothesised that a complex geometry may lead to interesting residual stress distributions that are quite different from simple cuboids, which forms the motivation for this research.

A comprehensive treatment of the complementary effects of residual stress and microstructure on the mechanical properties in H282, particularly E-PBF fabricated H282, is not yet available. Residual stresses within AM builds have been shown to significantly limit the fabricability of metal alloys, due to delamination from the build plates, as well as impact the tensile and fatigue properties of parts [12,17–21]. Though E-PBF has been touted as a method that significantly reduces residual stresses upon fabrication compared to other AM techniques such as laser powder bed fusion (L-PBF), E-PBF superalloys commonly exhibit reduced tensile properties in comparison to their L-PBF counterparts [12,21]. Furthermore, past AM H282 studies have only considered simple cuboidal builds, and limited microstructure-property considerations of thin walled struts [8–11]. However, AM thin-walled structures are commonplace in aerospace applications, such as in combustion chambers or in turbine blades [22,23].

In this publication, the residual stress distributions and their origins in an E-PBF processed H282 alloy build containing thin wall struts of varying thicknesses and internal 'cube' voids are reported. The influence of the residual stresses on microstructure-property relationships were also studied. The above characterisations were performed in representative locations of interest within an E-PBF H282 monolith. Nano-indentation tests were used to evaluate local hardness. Neutron diffraction (ND) was used to measure residual stresses and to evaluate texture. A detailed hierarchical microstructural investigation was performed through scanning electron microscopy (SEM), transmission electron microscopy (TEM), high resolution scanning transmission electron microscopy (STEM), and atom probe tomography (APT). These results provide insights into the interplay of residual stresses and microstructural effects on the mechanical performance of E-PBF H282.

2. Methods

2.1. Material

The pre-alloyed, gas-atomised H282 powders were produced by Praxair Inc. The powder composition was measured by inductively coupled plasma atomic emission spectroscopy (ICP-AES) and combustion analysis. The composition of the powder was Ni-22.22Cr-10.24 Co-5.24Mo-3.32Al-2.52Ti-0.67Fe-0.39Si-0.24 C-0.18 O-0.05B-0.01 V (at %). Other impurities (Mn, N, P, S, Nb, Cu) were measured to be < 0.15 at %. The mean powder diameter was measured to be 38.28 ± 1.66 μm, through SEM image analysis (Fig. 1); more details are presented in Section 2.3. Although some of the powder particles contain satellite morpholine (due to imperfect gas atomisation [24]), the mean powder circularity, calculated via Eq. (1), was measured to be 0.83 ± 0.45E-3. All measurement errors and error bars reported are 95% CI.

$$circularity = 4\pi \cdot Area \cdot Perimeter^{-2} \tag{1}$$

2.2. Print parameters and build geometries

H282 builds containing 'cube' internal voids as well as thin wall struts (Fig. 2) were fabricated in an Arcam Q10 machine (GE Additive) operated at 60 kV. The thin wall struts located on the top *xy*-surface were labelled TW1, TW2, and TW3 from thickest to thinnest (Fig. 2a-c). This build geometry was devised to investigate the effects of varying thermal conditions within different regions and thin wall widths of a singular build. The hypothesis behind using internal voids was to reduce mechanical restraints that will lead to relaxation of residual stresses.

These builds were printed simultaneously in a group of 12 builds. The builds were fabricated on a 304 stainless steel base plate using a 'random' spot melt pattern, where each point on a layer has an equal probability of being melted, but not necessarily in a sequential manner. Layer thicknesses were maintained at 50 μm, with no focus offset and a dwell time of 0.3 ms. The build plate temperature was initially set at ~1000 °C, equal to γ' solvus temperatures for H282 [6]. However, as a thermocouple was used to set/measure the bed temperature (as part of the Arcam Q10 system), there was uncertainty in the real base plate temperature during fabrication. Temperature uncertainties have been shown to be up to 200 °C in previous E-PBF studies [25]. After fabrication, builds were cooled to room temperature at a rate of ~161 °C/h and removed from the base plate by electrical discharge machining. A log of the machine conditions during fabrication can be found in the supplementary material (Fig. S1).

All microstructural analyses performed herein are from the regions that are far from the stress relieving cube voids. Regions of interest for microanalysis (indicated on Fig. 2c) include: • 2.5 mm from the top of TW1 and TW2 (i_{TW1}, i_{TW2}), • 7.5 mm from the top of TW1 (ii_{TW1}), • 10 mm from the top of TW1 and TW2 (iii_{TW1}, iii_{TW2}), • 2.5 mm from the top-centre of the build bulk; base of TW1, TW2, and TW3 (*iv*) and, • 2.5 mm above the bottom-centre of the build bulk (*v*).

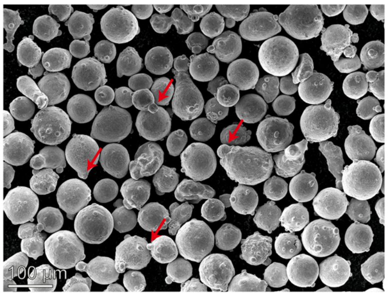

Fig. 1. SEM SE2 (secondary electron) micrograph of Haynes-282 powder used in this study. Satelliting is present in the powder (annotated), with variations in size and morphology. This micrograph was used for image analysis.

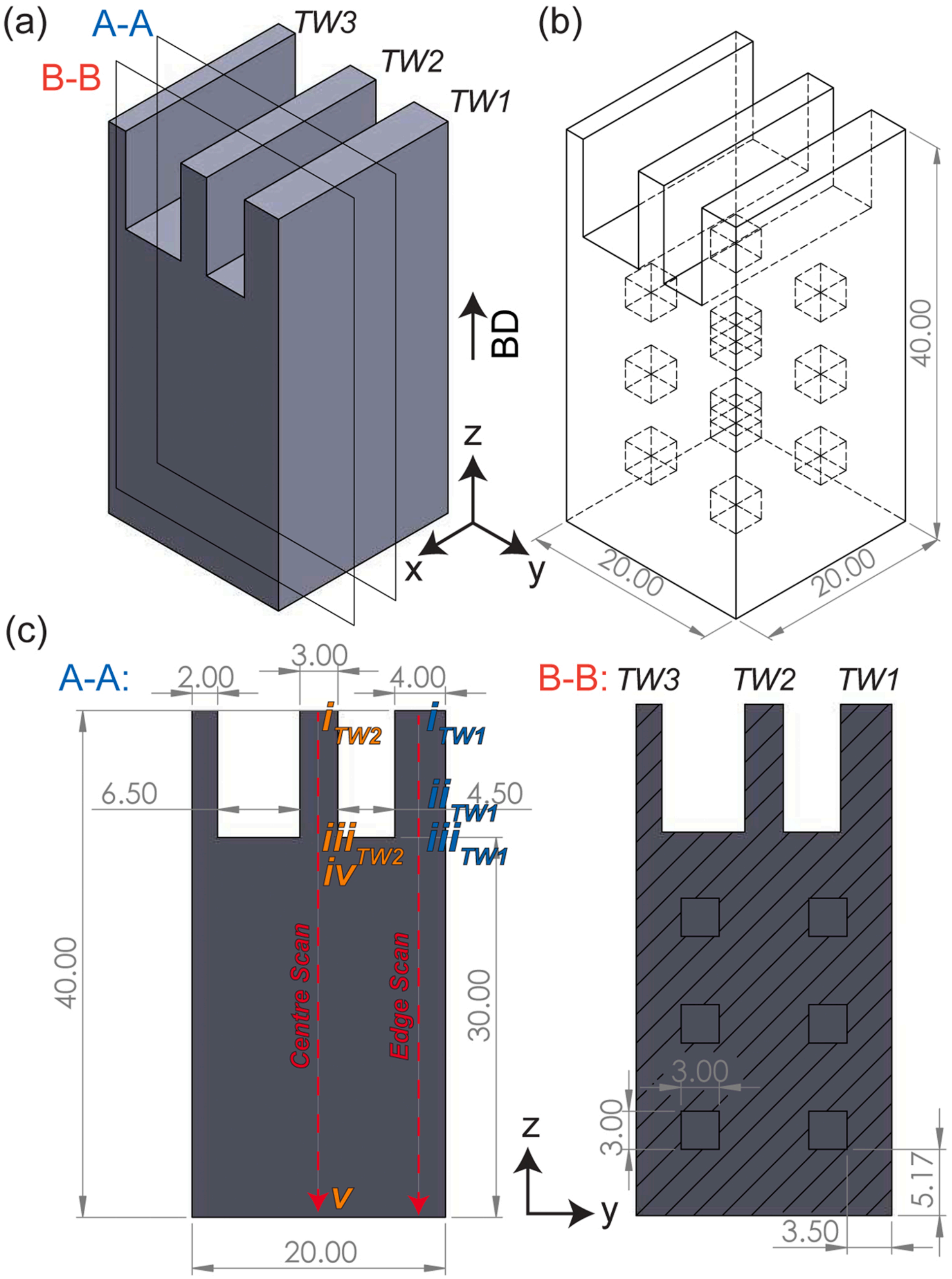

Fig. 2. (a) Schematic of E-PBF H282 build with reference to build direction (BD). (b) Skeleton view of E-PBF H2828 build, revealing internal cube void structures. (c) Schematic of cross-sectional views, (left) red arrows ND scan paths (edge and centre), and points of interest ($i_{TW1,TW2}$, ii_{TW1}, $iii_{TW1,TW2}$, *iv*, *v*) are notated for microscopy and microanalysis. (Right) Thin wall struts are labelled TW$_1$, TW$_2$, and TW$_3$ from thickest to thinnest.

2.3. Microstructural analysis

Samples were sectioned using a Struers Accutom-50 diamond saw from the central *yz*-plane (cross-section A-A in Fig. 2a & c).

Metallographic preparation of cut sections were prepared by mechanical grinding and polishing to a 0.25 µm finish. Subsequently, the specimens were polished to a 0.08 µm colloidal silica finish in a Buehler VibroMet2.

SEM was conducted using a Zeiss Sigma 3View field emission gun operating at 5 kV using a low kV Gatan backscattered electron (BSE) detector. Image analyses were performed with opensource software ImageJ v 1.53 c. A Gaussian blur of 1-pixel radii was applied followed by greyscale thresholding, and subsequent watershed segmentation. The above microstructural characterisations were performed at the points of interests: i_{TW1}, *iv*, and *v* (Fig. 2c).

Electron backscatter diffraction (EBSD) was performed in a Zeiss ULTRA Plus field emission SEM at 30 kV and a step size of 2 µm. The data was collected using an Oxford Instruments EBSD detector and processed using AZtecCrystal 2.0 software. A grain was defined as a group of at least 10 pixels and having a misorientation from surrounding crystals of at least 10°. The raw data was post-processed for rendering orientation maps by filtering for wild spikes and iterating to zero-solutions to the 5th nearest neighbours. The EBSD was performed on specimens containing positions i_{TW1}, ii_{TW1}, *iv*, and *v* (Fig. 2c).

SEM Energy dispersive x-ray spectroscopy (EDS) was performed in a Zeiss Sigma HD field emission SEM at 10 kV, with an oxford instruments EDS detector and processed using Aztec 5.0 software.

Standard techniques were used to electropolish TEM thin foils [26] from specimens containing positions i_{TW1}, iv, and v (Fig. 2c). These were mechanically polished to ~50 μm thickness on the xy-plane and electropolished in a Struers Tenupol using an electrolyte of 10% perchloric acid (vol.) in methanol at 15 V/− 30 °C. TEM and high resolution STEM micrographs were taken in a ThermoFisher Scientific double aberration corrected Themis-Z operated at 300 kV.

APT blanks (~0.5 x ~0.5 x ~20 mm^3) were sectioned from mechanically polished specimens on the xy-plane, containing positions i_{TW1}, iv, and v (Fig. 2c). These were electropolished into needle-shaped specimens using a standard 2-step electropolishing technique at room temperature [27]. Coarse polishing was performed using 25% perchloric acid (vol.) in acetic acid at 20 V, with fine polishing performed using 2–5% perchloric acid (vol.) in n-Butoxyethanol at 5–15 V. APT datasets were collected using a Cameca LEAP 3000-Si instrument, with a specimen temperature of ~25 K, a pulse rate of 200 kHz, a pulse fraction of 0.2, and a detection rate of 0.5% of an ion/pulse. The raw datasets were reconstructed in Cameca's Atom Probe Suite (APSuite) 6.1 software. The reconstruction was crystallographically calibrated using methods set by Gault et al. [28], at a detector efficiency of 57%. All reported APT datasets were background corrected.

2.4. Texture analysis

Neutron diffraction of this specimen for both the γ and γ' phases was completed at the High-Pressure-Preferred-Orientation (HIPPO) beamline at Los Alamos National Laboratory. All diffraction measurements were measured using a 10 mm diameter beam (probing multiple layers in one go), with an interaction volume of ~980 mm^3. Rotation angles of 0°, 67.5°, and 90° were used to capture representative diffraction events, and analysed at rotational positions for 20 min. HIPPO detector coverage provides 22.4% of the 2π pole figure hemisphere for a single rotation. These three rotations cover 51.2% of 2π which was sufficient for orientation distribution function (ODF) texture analysis, see Takajo & Vogel for details of angle selection [29].

Each specimen was analysed at the top (5 mm from top centre of build – encompassing TW1, TW2 and TW3), middle (20 mm from bottom centre of build), and bottom (5 mm from bottom centre of build) to evaluate texture changes with build height. These results were used to generate pole figures representative of global texture after processing using the Material Analysis Using Diffraction (MAUD) software package [30]. All textural neutron diffraction data was processed according to Saville et al. [31], with 7.5° pole figures exported from MAUD into the MATLAB plugin MTEX version 5.70. All presented pole figures were created with a 5° resolution ODF in MTEX [32].

2.5. Thermodynamic simulation

Thermodynamic simulation of equilibrium phase compositions was conducted using ThermoCalc 2021b software with the TC-Ni11 database. The calculations considered the pressure to be 0.7 Pa, corresponding to the measured chamber vacuum pressure during the E-PBF process (Supplementary material, Fig. S1).

2.6. Nanoindentations

Hardness was measured via instrumented indentation tests (nanoindentations) performed on the polished specimens in a Hysitron Ti 950 TriboIndenter (Bruker Corp.) equipped with a Berkovich diamond tip. An 11 mN load was used, with a loading/unloading rate of 1.1 mN/s and a dwell time of 10 s at max load. 10 rows of 10 indentations were performed (totalling 100 indentations), each spaced 5 μm apart to minimise cross-interaction of adjacent indentation strain fields, as per ASTM standards [33]. These measurements were restricted to the marked points of interest on the specimen ($i_{TW1,TW2}$, ii_{TW1}, $iii_{TW1,TW2}$, iv, v), as indicated in Fig. 2c. The Indentation direction aligns with x-direction of the build, i.e., perpendicular to the yz-plane. The unloading curves were analysed using methods described by Oliver-Pharr [33,34], with the upper 10% and lower 50% disregarded for curve fitting, as per ASTM standards.

2.7. Residual stress

Residual stress measurements were performed using the KOWARI strain scanner at the Australian Nuclear Science Technology Organisation (ANSTO) using a 2 × 2 × 2 mm^3 gauge volume. These were performed on builds fabricated with identical printing parameters and feedstock to those used for microscopy and microanalysis.

A monochromatic neutron beam with a wavelength of 1.498 Å was used. The detector angle, 2θ, was set correspondingly to the Ni(311) diffraction peak. 2 sets of line scans were performed along the build direction in the bulk of the as fabricated build. These scans were performed down the centre of the central thin wall strut (TW2) and thickest 'edge' thin wall strut (TW1), as indicated with red arrows in Fig. 2c. Scan centres were spaced 2.5 mm apart, with the initial scans beginning 2.5 mm from the top xy-surface.

The peak centre position in terms of scattering angle θ from the neutron diffraction pattern was determined by a pseudo-Voigt curve fit. The scattering angle was used to calculate the lattice spacing by Bragg's law:

$$n\lambda = 2d_{hkl}\sin\theta \tag{2}$$

Where, n is the order of the reflection plane, λ is the neutron wavelength, d_{hkl} is the lattice spacing, and θ is the angle between the incident beam and the scattering planes. From the lattice spacing, the residual lattice strain was calculated using the following equation:

$$\varepsilon = \frac{d_{hkl} - d^0_{hkl}}{d^0_{hkl}} \tag{3}$$

where, d^0_{hkl} is the strain-free lattice spacing for the hkl planes. Due to the lack of strain-free samples, this was calculated through assuming plane strain conditions along the z direction at the top of the 2 thin wall struts considered (positions i_{TW1} and i_{TW2}, Fig. 2c) [35]. A mean d^0_{hkl} of 1.082 ± 8.39E-05 Å from the 2 positions was used. It is important to note that as line-scans were performed, force and moment balances for validating d^0_{hkl} calculations were not possible [36]. Though d^0_{hkl} is also affected by changes in chemistry through the build [35], as shown in further detail in Section 3.4, phase chemistries remained similar throughout – unlikely changing d^0_{hkl} as a function of build height. Residual strain measurements were obtained on the bulk as-fabricated builds along the build direction in three principal directions (ε_{xx}, ε_{yy}, ε_{zz}).

The residual stress in three principal directions (σ_{xx}, σ_{yy}, σ_{zz}) was thus determined using Hooke's law:

$$\sigma_{xx} = \frac{E}{(1+\nu)(1-2\nu)}\left[(1-\nu)\varepsilon_{xx} + \nu\left(\varepsilon_{yy} + \varepsilon_{zz}\right)\right] \tag{4}$$

an elastic modulus, E, of 203 GPa and Poisson's ratio, ν, of 0.31 was measured from the Ni(311) reflection at position i_{TW2} (Fig. 2c), using a Voigt-Reuss-Hill mixtures model [37,38].

Equivalent von-Mises yield stresses (σ_{vm}) and hydrostatic stresses (σ_h) were also considered. These were calculated as follows:

$$\sigma_{vm} = \sqrt{\frac{(\sigma_{xx} - \sigma_{yy})^2 + (\sigma_{yy} - \sigma_{zz})^2 + (\sigma_{zz} - \sigma_{xx})^2}{2}} \tag{5}$$

$$\sigma_h = \frac{\sigma_{xx} + \sigma_{yy} + \sigma_{zz}}{3} \tag{6}$$

the calculated von-Mises yield stresses were independent of d^0_{hkl} assumptions, due to subsequent subtractions of the principal stresses.

Furthermore, as the same d^0_{hkl} was used for all calculations, the overall residual von-Mises stress trends observed holds true, though the absolute values reported may differ from the physical value.

3. Results

3.1. Grain characteristics

EBSD inverse pole figure (IPF) maps along the build direction (BD) reveal consistent columnar grain growth towards the BD throughout the entirety of the build, as seen in locations i_{TW1}, ii_{TW1}, *iv*, and *v* (Fig. 3a–d). The grains were larger than ~3 mm in length and ~200 µm in width. There was little variation in mean grain size or aspect ratio in all locations. The corresponding EBSD pole figures show that the grains were strongly {001} textured (along the BD) with little change in the degree of texturing with build height. Though some equiaxed grains could be seen at the bottom of location *v*, Fig. 3d, these were a result of partially sintered powder at the bottom of the build. Kernel average misorientation (KAM) maps from the EBSD scans (Supplementary Fig. S2) also showed minimal changes in misorientation with build height.

To investigate the overall textural behaviour of γ and γ′ individually with build height, pole figures were obtained via ND at various locations in the build height. Their individual textures remained unchanged with build height; a representative figure is shown in Fig. 4. Consistent fibre texture around the build direction was observed for γ of ~6–7 multiples of uniform distribution (m.u.d.). Whilst γ′ texture exhibited a typical cube texture that was rotate ~15–20° around the build direction of ~8 m.u.d.

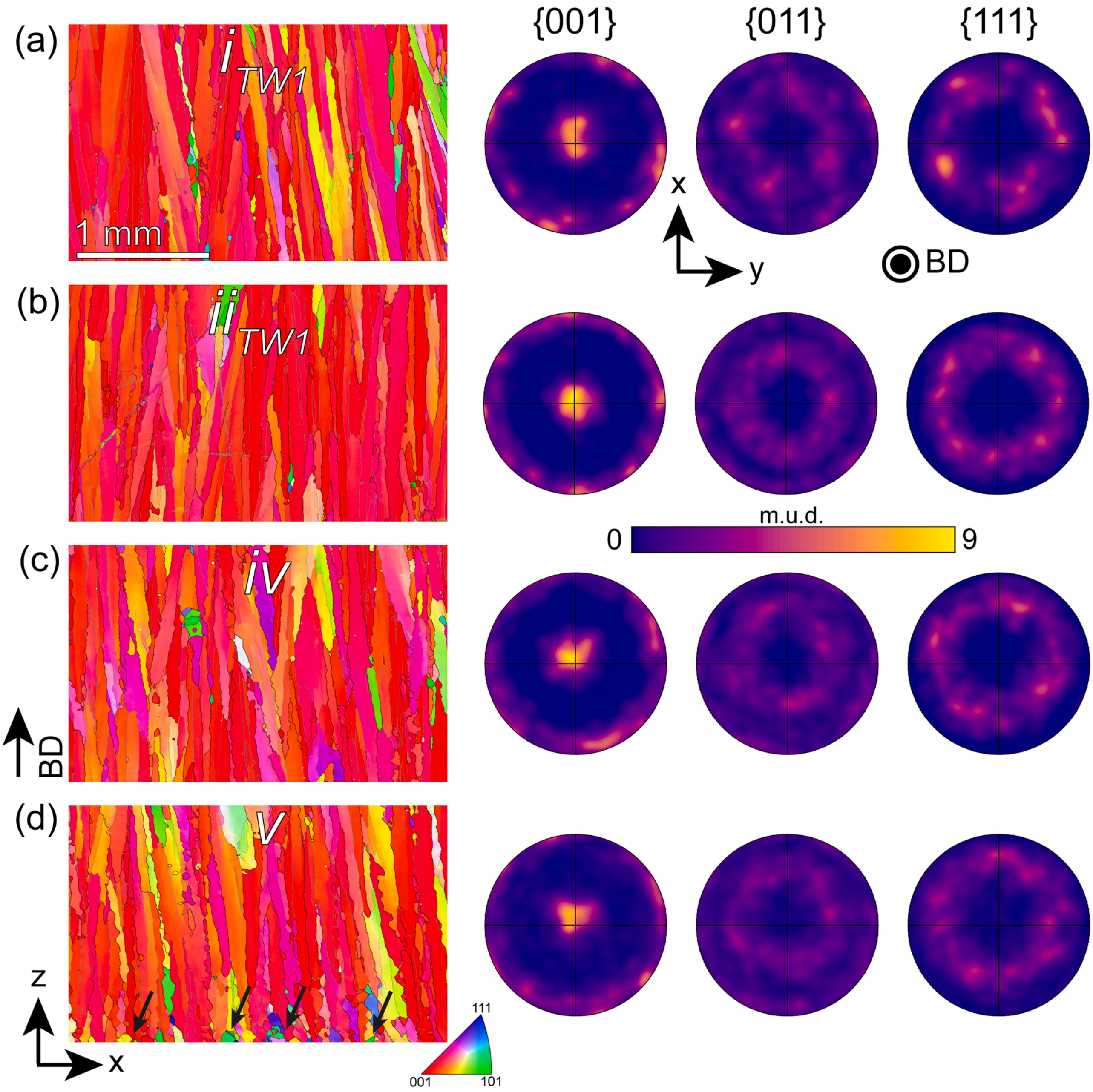

Fig. 3. (Left) IPF maps along the BD and (right) associated pole figures at points of interest, (a) i_{TW1} (b) ii_{TW1}, (c) *iv* and (d) *v*. Equiaxed grains are notated in (d). Outlined in black are high angle grain boundaries (≥ 20°) and in grey are low angle grain boundaries (≥ 2 – 20°). Pole figures were contoured with 10° halfwidths and cluster sizes of 5°.

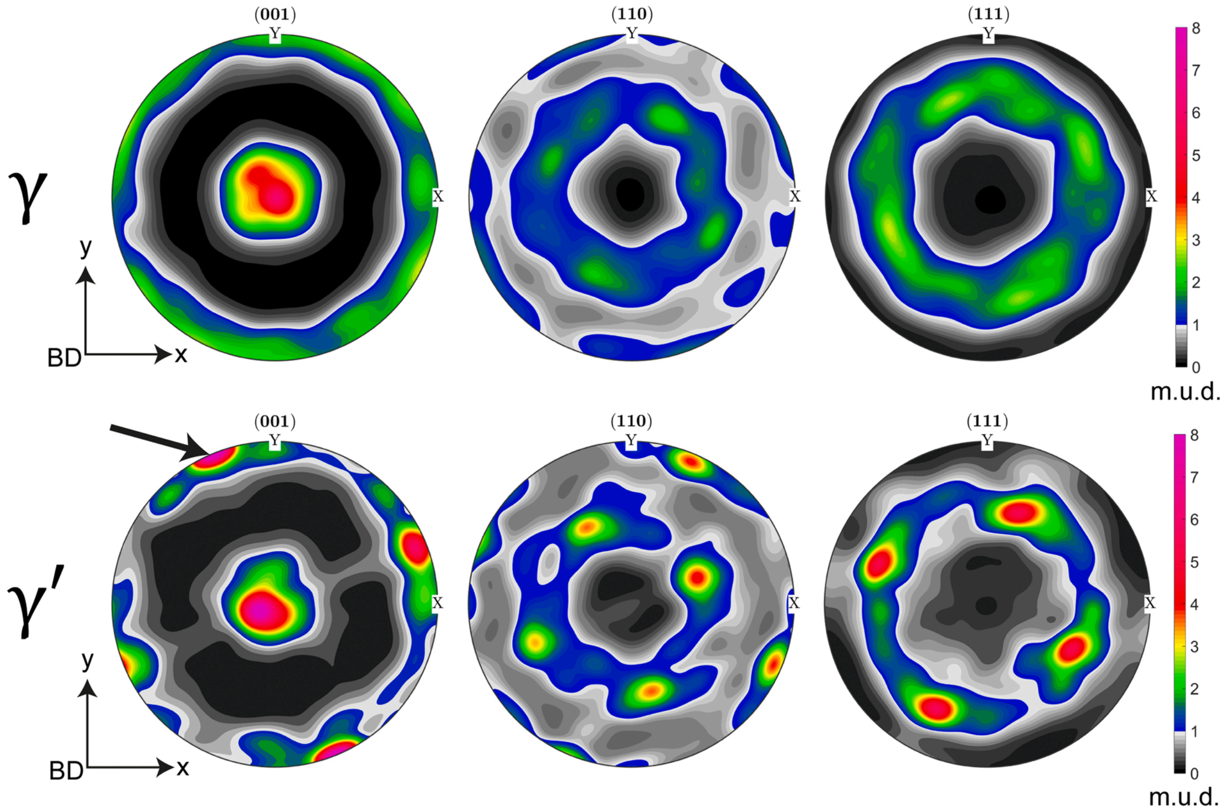

Fig. 4. Representative pole figures measured from the centre of the build via neutron diffraction using a 10 mm diameter beam. Consistent fibre texture around BD was observed for γ. The γ' phase exhibited a cube texture rotated by ~15–20° from typical orientations. These textures were consistent with build height.

3.2. γ' morphology

SEM BSE micrographs show extensive distribution of cuboidal primary γ' precipitation and carbides (Fig. 5). These were performed only at locations interest: • top of TW1 (i_{TW1}), • 2.5 mm from the bottom of TW1 (ii_{TW1}); corresponding to the hardness spike seen in Table 3, • top-centre of the build bulk (*iv*) and, • bottom-centre of the build bulk (*v*). The carbides were identified as Mo,Ti,Ta-rich carbides via SEM EDS analysis (Fig. 6) and were not considered for further analysis.

Primary γ' sizes were determined using equivalent spherical diameters via image analysis, and their phase fractions were assumed to be equivalent to the measured area fractions. Aspect ratios and circularities were similarly measured via image analysis. Although, the primary γ' size linearly reduces by 33.7% with increasing build height (*v* to i_{TW1}), the primary γ' phase fraction increases by 9.0% (Table 1). This suggests that the number density of γ' may be higher in the top of the build. Furthermore, their aspect ratios and circularities, indicate that primary γ' morphology remained consistently cuboidal throughout the build, with a slight reduction in circularity at position *v*.

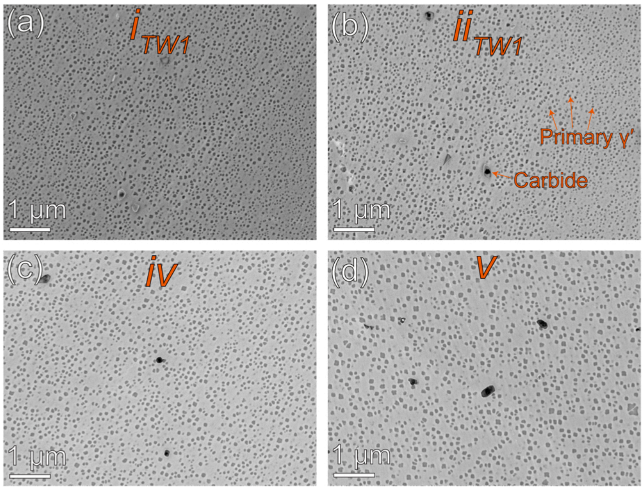

Fig. 5. BSE SEM micrographs showing primary γ′ (darker contrast) and carbides (black) at points of interest (a) i_{TW1}, (b) ii_{TW1}, (c) *iv*, and (d) *v*. These micrographs were used for image analysis.

Displaced aperture dark field (DF) TEM micrographs of i_{TW1}, *iv*, and *v* were taken (Fig. 7a–c) near 2-beam conditions using a superlattice (γ') diffraction spot. These are forbidden face-centred cubic (FCC) reflections, not shown when γ' is absent [26,39]. Spherical secondary γ' precipitation (<5 nm in diameter) was found to be present throughout the entirety of the build. Fig. 7d & e displays representative low and high magnification STEM high angular annular darkfield (HAADF) micrographs of position *iv* taken along a < 110 > zone axis, also showing evidence of secondary γ' precipitation. Resolving secondary γ' was difficult via HAADF STEM due to Z contrast contributions by the surrounding γ matrix, nonetheless, this was indicative of bimodal primary and secondary γ' precipitation in E-PBF H282.

3.3. Dislocation densities

To evaluate the role of defects on the hardness variations, brightfield (BF) TEM micrographs (Fig. 8) at locations i_{TW1}, *iv*, and *v* show the dislocation distributions at various magnifications. All specimens were tilted to a < 110 > zone axis and imaged at 2 beam conditions to facilitate dislocation observations. In all regions, low densities dislocations were observed and qualitatively similar, not interacting with or shearing γ′ precipitates. Low amounts of sub-grain boundaries were also observed to have formed. This was surmised to be from dislocation recovery within γ grains [40] during the cyclic heating and cooling E-PBF process.

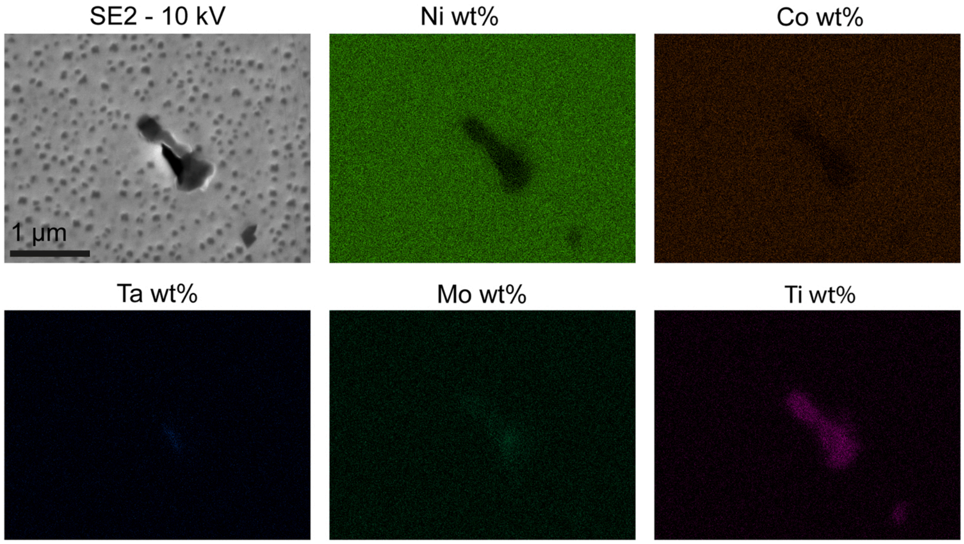

Fig. 6. Representative SE2 micrograph with EDS maps (from location *v*) of Mo,Ti,Ta-rich carbides found throughout build.

Table 1

Variations in primary γ' size, phase fraction, aspect ratio, and circularity at positions i_{TW1}, ii_{TW1}, *iv*, and *v*, within the build. Determined via image analysis of Fig. 5.

	Primary γ' size (nm)	γ' phase fraction (%)	Aspect Ratio	Circularity
i_{TW1}	54.0 ± 1.4	18.3	1.27 ± 0.01	0.96 ± 2.46E-03
ii_{TW1}	58.4 ± 1.7	18.1	1.25 ± 0.01	0.97 ± 2.09E-03
iv	68.6 ± 2.3	17.0	1.24 ± 0.01	0.96 ± 2.45E-03
v	81.4 ± 3.3	16.5	1.28 ± 0.01	0.93 ± 3.79E-03

3.4. γ/γ′ phase chemistry

APT was employed to analyse the effects of possible variations in phase chemistries on the measured hardnesses. Fig. 9 shows characteristic atom maps at locations i_{TW1}, *iv*, and *v*. γ and primary γ′ chemistries were determined through bulk measurements of isoconcentration surfaces of Cr = 25.15 at% and Al + Ti = 20.80 at%, respectively (Table 2). These isoconcentration surface values were determined via methods published by Theska et al. [41], eliminating interfacial contributions to measured chemistries. 6 at% Al + Ti isoconcentration surfaces were used to delineate secondary γ′, confirming DF TEM observations. Due to their small sizes (<5 nm), causing interfacial contributions to measured bulk chemistries [42], secondary γ′ chemistries and effects were not considered in this study. Bulk γ and primary γ′ compositions were aggregated and averaged over 3 different datasets for each region, with a minimum of 10 million ions for each phase reported.

There was little variance in primary γ′ chemistries throughout the build. Al and Ti concentrations in γ varies slightly between regions. Al

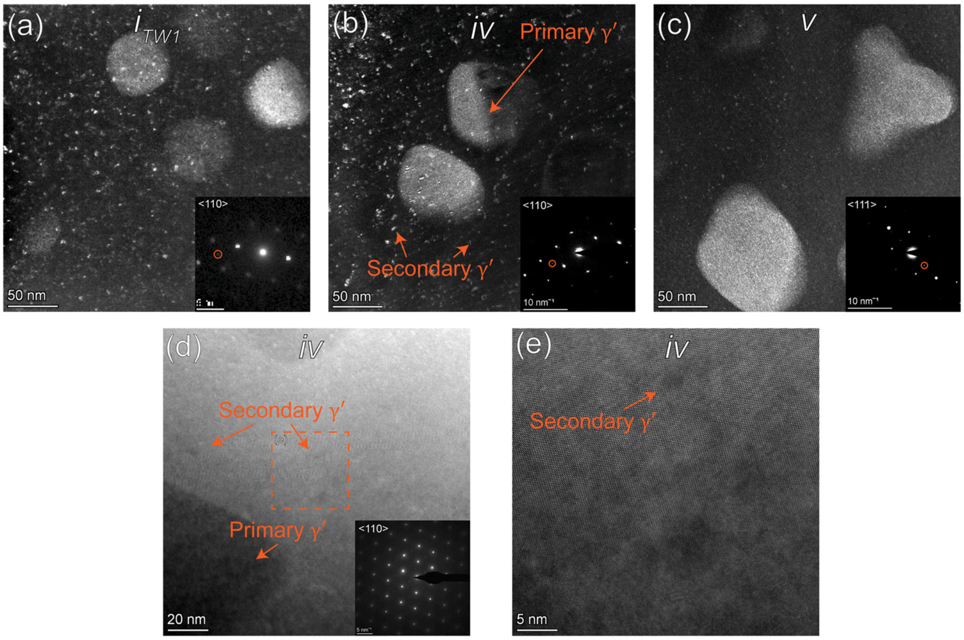

Fig. 7. Displaced aperture DF TEM micrographs formed with superlattice spots, taken near 2-beam conditions for locations (a) i_{TW1}, (b) *iv*, and (c) *v*. Primary and secondary γ′ precipitation is seen in all locations. Insets are the corresponding DPs with the superlattice spots (forbidden FCC reflections) used to form the DF micrograph indicated in red circles. Representative STEM HAADF micrographs taken along < 110 > zone axis for location *iv* at (d) low and (e) high magnification, also showing primary and secondary γ′ precipitation.

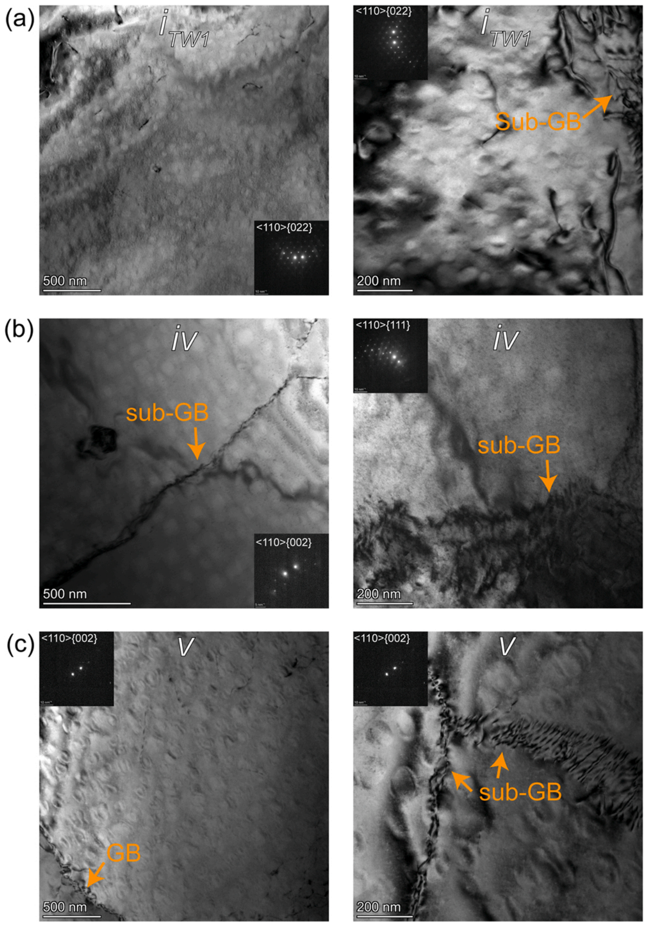

Fig. 8. BF TEM micrographs taken at two beam condition showing low dislocation densities. Taken at low magnification (left) and higher magnification (right) at points of interest (a) i_{TW1}, (b) *iv*, and (c) *v*. Sub-grain boundaries were formed resultant from dislocation recovery due to cyclic E-PBF heating and cooling process.

concentration in γ was highest at location i_{TW1}, followed by *v,* and *iv*. Conversely, Ti concentration in γ was lowest in location i_{TW1}, followed by *iv,* and *v*. Proximity histograms (proxigrams) were applied to the 20.80 at% Al + Ti isoconcentration surfaces, from the representative atom maps (Fig. 9). A bin size of 0.5 nm was used, and proxigrams were concurrently applied and averaged over all isoconcentration surfaces for statistical significance. As viewed in Fig. 10, these show expected enrichments and depletions of solutes to primary γ′, but no solute segregation behaviour at primary γ′/γ interface boundaries.

Equilibrium phases calculated by ThermoCalc are shown in Fig. 11. The preheat temperature (~1000 °C) was found to be at γ′ solvus. This suggests that the majority of γ' precipitation only occurred upon continuous cooling to room temperature. However, due to uncertainty of the measured bed temperature, and the gradient of γ′ sizes with build height (Table 1), the authors surmise that γ′ precipitation and coarsening also occurred during fabrication. The equilibrium composition of γ and primary γ′ was calculated as the mean composition between 728 and 810 °C (Table 2). This temperature range corresponded to the maximum and minimum primary γ′ phase fractions, respectively, determined via SEM (Table 1), also giving prudence to the postulation of in-situ precipitation at lower temperatures. There was little variance in predicted chemistry within this range. 1.5% phase fraction of M_6C carbides was also predicted to form at this temperature range.

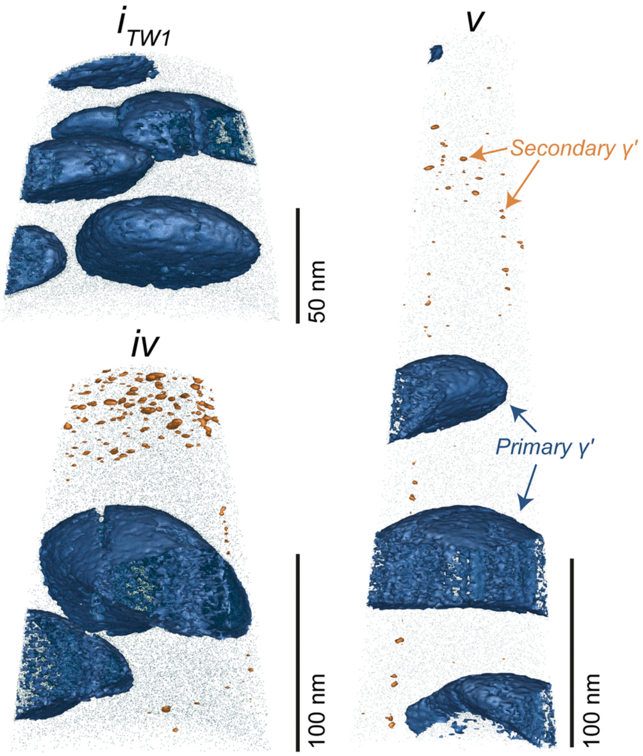

Fig. 9. Representative atom distribution maps of Ti for locations i_{TW1}, *iv* and *v*. In blue, 20.80 at% Al + Ti isoconcentration surfaces showing primary γ′ precipitation. In orange, 6.00 at% Al + Ti isoconcentration surfaces delineate secondary γ′ precipitation.

3.5. *Hardness*

Nanoindentations were performed at the locations of interest corresponding to Fig. 2c. The results, summarised in Table 3, show an increase in hardness with build height (from *v* to i_{TW1}). Of note was a spike in hardness at location ii_{TW1}. There was little observable variation between the bottom top and top of the thickest, thin wall strut, TW1 (iii_{TW1} and i_{TW1}, respectively), nor within the bulk of the builds (*v* and *iv*, respectively). However, there was an 8.1% increase in hardness from the bottom to the top of TW2 (iii_{TW2} and i_{TW2}, respectively).

3.6. *Residual stress*

Residual stresses were measured to understand the spike in hardness measured at position ii_{TW1}. The principal and hydrostatic residual stress distributions show an increasingly compressive behaviour with increasing build height for both edge and centre scan paths (Fig. 12a, b & d). Apart from position $ii_{TW1,}$ there was a slight increasing trend in equivalent von-Mises yield stress (σ_{vm}) with increasing build height (Fig. 12c). At location ii_{TW1}, the spike in von-Mises residual stress was due to a spike in residual tensile stress along the *x*-axis (σ_{xx}). This was the direction along the length axis of TW1 (Fig. 2c). Exclusive of ii_{TW1}, the residual stress distributions along TW1 & TW2 mimic each other.

This spike in residual stress magnitude seen in Fig. 12c at ii_{TW1}, correlated with increased hardness measured by nanoindentation. Furthermore, the overall increased hardness with build height, corresponds with increased tensile residual stresses toward the top of the build (Fig. 12a & b).

4. Discussion

The as-built E-PBF H282 monoliths showed complex residual stress distributions, resultant from the cyclic rapid heating and cooling process

Table 2
Nominal bulk H282 composition obtained from ICP-AES and combustion analysis of pre-alloyed powder. Calculated equilibrium compositions by ThermoCalc, and measured compositions by APT of γ and primary γ′ at locations i_{TW1}, *iv* and *v*. Calculated compositions taken as an average of predicted compositions between 728 and 810 °C. Only errors (95% CI) > 0.01 at% are reported.

at%	Nominal	γ				Primary γ'			
		Calculated	i_{TW1}	*iv*	*v*	*Calculated*	i_{TW1}	*iv*	*v*
Ni	54.77	52.16 ± 0.15	52.87	53.49	54.9	70.71 ± 0.04	69.91	69.41	69.8
Cr	22.22	26.97 ± 0.16	29.2	27.75	26.62	1.22 ± 0.02	2.12	3.35	2.75
Co	10.24	11.84 ± 0.05	10.59	10.4	9.99	3.96	2.26	2.79	2.59
Al	3.32	1.56 ± 0.09	1.62	0.88	0.97	11.55 ± 0.10	12.38	11.62	11.63
Ti	2.52	0.37 ± 0.05	0.67	1.99	2.05	12.23 ± 0.09	11.22	10.25	10.66
Mo	5.24	5.71 ± 0.02	4.17	4.63	4.62	0.15	1.9	2.33	2.33
Si	0.39	0.48	0.1	0.12	0.12	0.01	0.08	0.08	0.09
C	0.24	0.01	0.06	0.05	0.04	–	0.01	0.01	0.01
Fe	0.67	0.81	0.64	0.64	0.63	0.09	0.08	0.11	0.09
Mn	0.04	0.05	0.02	0.02	0.02	0.01	0.01	0.01	0.01
B	0.05	–	0.02	0.01	0.01	–	0.02	0.02	0.02
V	0.01	0.01	0.03	0.03	0.03	–	0.02	0.01	0.02
Others	< 0.28	0.01	–	–	–	0.07	–	–	–

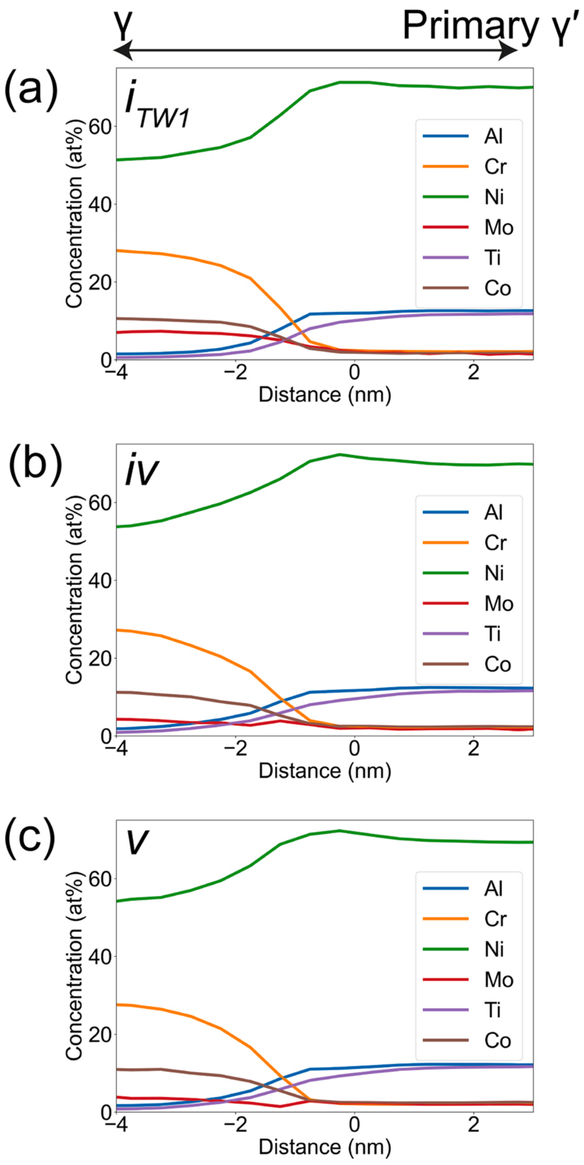

Fig. 10. Proxigrams of major constituent elements (Al, Cr, Ni, Mo, Ti, and Co) of primary γ′ for locations (a) i_{TW1}, (b) *iv*, and (c) *v*. Performed on 20.80 at% Al + Ti isoconcentration surfaces in Fig. 9. Errors < 0.01 at% for all elements.

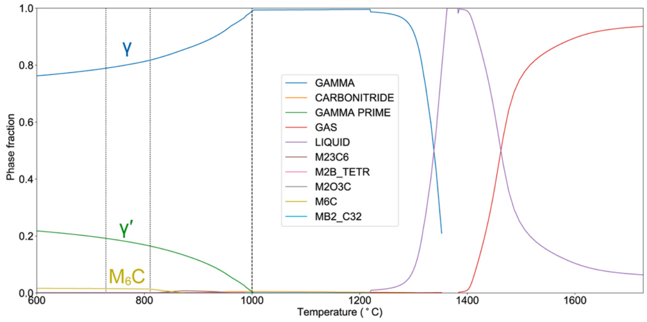

Fig. 11. Equilibrium phases of H282 at different temperatures, calculated through ThermoCalc using the TC-Ni11 database. Dashed line represents the E-PBF preheat temperature (1000 °C). Dotted lines represent temperature ranges (728–810 °C) of equivalent γ′ phase fractions determined via SEM (Table 1).

Table 3
Hardness (GPa) measurements via nanoindentation captured at all positions of interest indicated in Figs. 2c and 12.

GPa	i_{TW1}	ii_{TW1}	iii_{TW1}	i_{TW2}	iii_{TW2}	*iv*	*v*
	4.88 ± 0.02	5.95 ± 0.13	4.85 ± 0.03	4.79 ± 0.04	4.40 ± 0.17	4.59 ± 0.02	4.52 ± 0.02

during fabrication and the complex geometry. The complex interplay between geometry, process, and material phenomenon might have contributed to the combination of residual stress, microstructural and hardness variations observed through the build. The residual stress distributions within the build will be discussed regarding their origins and influence on microstructure and properties.

4.1. Origins of residual stress variations

Residual stresses are largely characterised among the length scales upon which they act. They are loosely grouped as type I (macro), type II (micro), and type III (nano) [43]. The drivers for the above include plastic deformation gradients brought about by thermal stresses (type I), intragranular or phase transformation stresses (type II) and dislocation stress fields (type III). Though type I residual stresses are the main contributors in metal AM [44], type II and type III are often non-zero and revealed via other techniques such as high spatial resolution microscopy and high energy synchotron X-ray diffraction [45]. Due to volumetric averaging effects and resolution limits (~500 µm) of neutron diffraction, only type I and type II residual stresses were directly measurable [43,44]. This eliminates type III residual stress origins from the reported

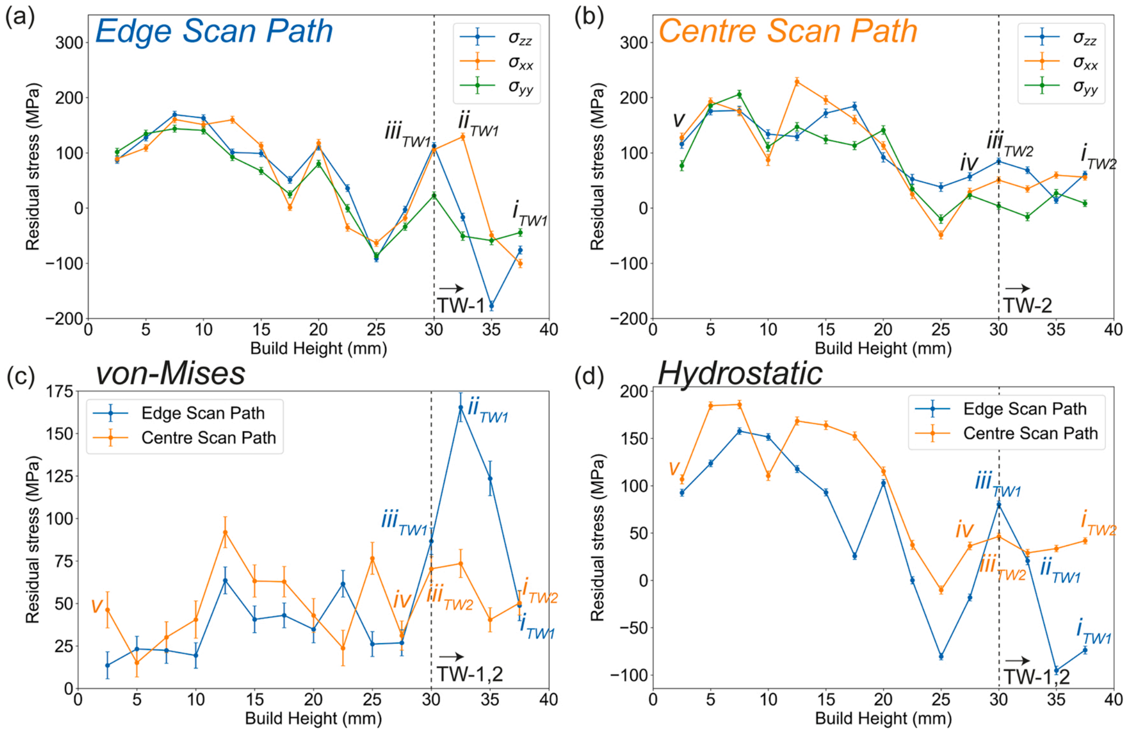

Fig. 12. Principal residual stress (σ_{xx}, σ_{yy}, σ_{zz}) distributions along (a) edge path scan (along TW1) and (b) centre path scan (along TW2), captured through neutron diffraction. (c) von-Mises yield stress and (d) hydrostatic stress magnitudes are shown for both edge and centre scan path. Annotated are the equivalent positions of interest shown in Fig. 2c.

residual stress distributions in Fig. 12. Deconvolving type I and type II residual stresses require subsequent residual stress measurement techniques purely for type II contributors such as high resolution EBSD strain mapping [46], though was outside the scope of this study.

For type II residual stresses, the possible contributing factors include the variations in γ' shape, size, and phase fractions, as well as γ grain characteristics. The precipitation of spherical secondary γ' observed (Fig. 7 & Fig. 9) was unlikely to contribute to the measured residual stresses (Fig. 12); as well known in Ni-based superalloys, spherical γ' result in near nil γ/γ' lattice mismatch [39]. The cuboidal primary γ' morphology through the build (Fig. 5) do not have nil-lattice mismatch and hence would exhibit (type II) lattice strains. The authors postulate that this was the reason for the observed ~15–20° rotation from cube texture observed via ND (Fig. 4). Though indicative that a degree of type II residual stress contribution was from cuboidal primary γ', as γ' texturing behaviour was observed to be unchanged through the build height, its contribution through the build could similarly be surmised as constant throughout the entire monolith.

Fibre textured γ grains with high proportions of high angle GBs can be significant indicators of type II residual stresses [19,43]. Although, the residual stress distributions i_{TW1}, ii_{TW1}, iv and v vary significantly (Fig. 12), there were no equivalent observed textural variations via ND (Fig. 4). Furthermore, although a $2 \times 2 \times 2$ mm^3 gauge volume was used for residual stress measurements; resulting in reduced γ grain statistics, there were little changes in columnar γ grain characteristics throughout the build as measured by EBSD (Figs. 3 and S2). Hence, the authors conclude that type II residual stresses were similar through the entire monolith, contributed by γ and primary γ'. This eliminates type II residual stresses as a major contributory factor to the variations in residual stress distributions observed.

As such, by elimination, type I residual stresses were the prominent factor in this E-PBF H282 build (resultant from the AM process) to the variations in residual stresses observed (Fig. 12). This was owing to the cyclic heating and cooling process associated with the layer build up process, as well as the geometry of the build [12,44,47]. Previously melted material experiences remelting and re-solidification cycles, leading to multiple instances of expansion and contraction. This corresponds to cycles of compressive stresses at the heat affected zone and tensile stress when the power source is removed [47–49]. The residual type I compressive or tensile stresses were resultant from imbalanced stress tensors due to these cycles. These thermal-stress cycles reduce in number with successive build layers, resulting in variations in thermal signature, hence supporting the observed residual stress distributions.

Furthermore, exclusive of position ii_{TW1}, the authors attribute the overall reduction in von-Mises residual stress toward the bottom of the builds (v) in comparison to the top of TW1 (i_{TW1}) and TW2 (i_{TW2}), as seen in Fig. 12c, to longer periods of 'intrinsic' stress relief annealing toward the bottom of the build during the E-PBF process.

4.2. Residual stress spike

The spike in residual stress magnitude at ii_{TW1} was primarily due to a significant increase in tension for the σ_{xx} principal stress (Fig. 12a & c). It can be surmised that the spike in residual stress at ii_{TW1} (unseen at the equivalent position in TW2, Fig. 12a & b) was due to thin wall thickness effects. Upon initial depositions of the thin walls, at locations iii_{TW1} and iii_{TW2}, $\sigma_{yy} \approx 0$. This was expected as σ_{yy} has easier stress relief with shorter width (y) distance to the outer xz-edges (Fig. 2); as AM thin-walled geometries have greater residual stress relief toward the outer surfaces [50]. However, despite similar thin wall geometries iii_{TW1} exhibits higher residual stresses ($\sigma_{zz} \approx 120$ MPa, $\sigma_{xx} \approx 110$ MPa) than iii_{TW2}, ($\sigma_{zz} \approx 90$ MPa, $\sigma_{xx} \approx 40$ MPa) in the xz-plane.

The authors propose that the increase in wall thickness (y-direction) from 3 mm at TW2 to 4 mm at TW1 resulted in highly constrained thermal stress conditions (in TW1). As no changes in scan strategy occurred between thin wall struts, the increase in wall thickness, may result in decreased melt pool dimensions during fabrication [51], due to increases in heat accumulation and temperature gradients with reducing wall thicknesses. This results in smaller heat affected zones. Initially at iii_{TW1}, there was an accumulation of tensile stresses from the solidification fronts of these 'smaller' heat affected zones [47–49], as the energy input remained unchanged. This accumulation works in tandem with the tensile stresses common near the outer edges of PBF builds [12, 36]. The authors postulate that with successive build layers, stress relief was achieved along the *z*-direction (toward the top *xy*-face of the build) in TW1. At location ii_{TW1}, the opportunity for stress relief along the *x* direction to the outer *yz*-facing edges remains limited. At ii_{TW1}, this resulted in σ_{zz} reducing to $\sim-$ 10 MPa and σ_{xx} increasing to ~140 MPa. As the residual stress along the *x*-axis was not yet relieved, this resulted in the spike in von-Mises residual stress seen in Fig. 12c. With subsequent build layers, the residual tensile stresses originating from the build layers below further relax, resulting in similar residual stress profiles between i_{TW1} and ii_{TW1}.

4.3. Interplay between hardness and residual stress

Complex scan strategies, print parameter sweeps and elevated bed temperatures are commonly employed in PBF processes to reduce type I residual stresses, as these are reported to be the leading contributors toward a reduction in mechanical performance in metal AM [12,17–19]. However, from Fig. 12c, the mean von-Mises residual stress along the edge scan path (along TW1 & inclusive of ii_{TW1}), and centre scan path (along TW2) were: 53.31 ± 20.74 MPa and 50.60 ± 10.41 MPa, respectively. Although E-PBF is often touted as a process that reduces residual stresses [12,36], this was still a significant amount as the 0.2% yield strength and ultimate tensile strength of heat treated conventionally cast H282 are 765 MPa and 1255 MPa, respectively [52]. The residual stresses along the edge scan path (at upper limit of uncertainties) can reach ~10% of the yield stress of H282, potentially reducing mechanical performance. However, it was observed that increased von-Mises residual stresses (Fig. 12c), irrespective of principal stress directions (Fig. 12a & b) resulted in an increased hardness (Table 3). Though to be reiterated, the increased hardness also co-correlated with variations in γ' morphology with build height (Table 1). Although hardness measurements via nanoindentations often overestimate the physical value, due to size effects, the relative comparisons are valid [53]. This observation was comparable with those from Chen et al. [19], wherein stress relief annealed L-PBF stainless steel builds had reduced tensile properties, when compared to as-fabricated builds containing either tensile or compressive residual stresses.

This phenomenon was further emphasised in the significant spike in residual stress at position $ii_{TW1,}$ occurring ~7.5 mm from the top of TW1 (Fig. 12a and c). This correlates with the highest measured hardness within the build of 5.95 GPa (Table 3).

Precipitate strengthening imparted by γ' precipitation within the γ matrix is the main mechanism for strengthening in Ni-based superalloys [39]. However, precipitate characteristics do not correlate with the spike in hardness at position ii_{TW1}; as primary γ' sizes reduced linearly with build height (Table 1). Furthermore, there was little variation in mean γ grain size, aspect ratio or texturing in all locations, inclusive of ii_{TW1} where the spike in hardness was measured (Fig. 3 & Fig. 4).

Possible other contributory causes thus also include type III residual stress sources, such as changes in dislocation density or phase chemistry at this location. However, BF TEM micrographs (Fig. 8) show minimal dislocation densities at various positions throughout the build. Furthermore, the presence of sub-grain boundaries due to dislocation recovery was indicative of reduced type III residual stresses after reheating. Thus, the authors surmise that the spike in hardness measured at ii_{TW1} was not correlated to any changes in γ' precipitation, γ grain characteristics, or dislocation behaviour. Furthermore, the γ' phase chemistries measured by APT show no significant variations either through the build (Table 2). As such, the high hardness at ii_{TW1} (Table 3) was directly due to a spike in type I σ_{xx} residual stress at this location (Fig. 12a). As indentations occurred along the *x*-direction on the *yz*-plane, this resulted in higher resistance to deformation and hence a spike in hardness, due to the compressive nature of the nanoindentations.

Exclusive of ii_{TW1} hardness increases by 7.4% with build height (from position *v* to i_{TW1}), correlating with a reduction in primary γ' size by 39.4% and phase fraction increase by 9.9% (Table 1), and also an overall increase in compressive residual stresses with build height (Fig. 12). Though there were slight variations in predicted equilibrium phase chemistries and those measured by APT (Table 2), this was expected due to the non-thermodynamically equilibrium process of AM. It can be surmised that the overall hardness trend within the build (exclusive of ii_{TW1}) was majorly due to a combination of changes in type I residual stress distributions and primary γ' sizes & phase fraction with build height. Interestingly, many recent studies have pointed to variations in solute site occupancies in the $L1_2$ γ' structure being a contributor to property effects, even with no variations in bulk chemistries [54–57]. The effects of site occupancy variations on property contributions in this alloy will be analysed in future investigations.

Of note, the overall compressive residual stress distribution with increasing build height (Fig. 12a, b, & d), contrasts with what was commonly seen in E-PBF builds; whereby increasingly tensile stresses were expected toward the top of the builds [12]. The similar overall residual stress distributions for both edge and centre scans (Fig. 12a & b) was also contrary to expectations in E-PBF builds; wherein residual stresses tend to be compressive toward the centre (where the bulk of the heat during AM is retained during fabrication) and tensile at the edge (on the *xy*-plane) [12,36]. This was advantageous, as it further limits the possibility of delamination during fabrication and warping upon build removal from base plate. The authors postulate that residual stress relief due the inclusion of the internal voids were the primary contributors to changes in expected residual stress distribution behaviour. However, future work is required to evaluate the effects of the stress relieving voids. Furthermore, exclusive of position ii_{TW1}, it was found that the residual stress trend between TW1 and TW2 were similar, though differed in magnitude. This indicates that the 1 mm reduction in thin wall width from 4 to 3 mm, respectively, was sufficient to result in a measurable variation in localised residual stress distributions for E-PBF H282 thin wall struts. In the future, the residual stress of TW3 (2 mm width) will be considered.

5. Conclusions

The effects of the residual stress distributions of an as-fabricated E-PBF H282 build containing thin wall struts were investigated. Local hardness measurements and multi-scale microscopy & microanalysis show correlative behaviours between residual stresses and microstructure-property phenomena. The results lend themselves to informing future simulations and print strategies of E-PBF H282. The following specific findings were determined:

1. Type I (macro) residual stresses were the predominant contributors to the variations in residual stress distributions observed.
2. Principal residual stress distributions along line scans were increasingly compressive with increasing build height (bottom to top), with the equivalent von-Mises stress similarly increasing with build height.
3. Hardness measurements show similar increasing trends with increasing build height. The changes in hardness with build height were attributed primarily to a combination of type I residual stresses and γ' morphology.
4. Low dislocation densities were observed throughout the build, forming sub-grain boundaries. This was indicative of dislocation recovery and residual stress relief through the build.
5. A 1 mm reduction in thin wall thickness from 4 mm to 3 mm (TW1 to TW2) can cause significant localised changes in residual stress distributions and hardness, with a proposed mechanism being due to changes in highly constrained localised thermal stress conditions.

CRediT authorship contribution statement

Bryan Lim: Writing – review & editing, Writing – original draft, Visualization, Methodology, Investigation, Formal analysis, Conceptualization. **Xiaozhou Liao:** Writing – review & editing, Project administration, Funding acquisition. **Sophie Primig:** Writing – review & editing, Resources, Project administration, Funding acquisition. **Andrew J. Breen:** Writing – review & editing, Supervision. **Sudarsanam Suresh Babu:** Writing – review & editing, Resources. **Simon P. Ringer:** Writing – review & editing, Supervision, Project administration, Funding acquisition, Conceptualization. **Hansheng Chen:** Writing – review & editing, Validation, Methodology, Conceptualization. **Keita Nomoto:** Writing – review & editing, Investigation. **Zibin Chen:** Writing – review & editing, Investigation. **Alec I. Saville:** Writing – review & editing, Formal analysis. **Sven Vogel:** Investigation. **Amy J. Clarke:** Writing – review & editing, Resources. **Mark Reid:** Formal analysis. **Anna Paradowska:** Investigation.

Declaration of Competing Interest

The authors declare that they have no known competing financial interests or personal relationships that could have appeared to influence the work reported in this paper.

Data Availability

Data will be made available on request.

Acknowledgements

The authors acknowledg the facilities, the scientific, and technical assistance of the teams at Sydney Microscopy & Microanalysis (SMM) and the Sydney Manufacturing Hub, which are Core Research Facilities at the University of Sydney. SMM is the University of Sydney's node of Microscopy Australia. Mr. James Dingle's (University of Sydney) contribution to Figs. 2 and 12 are acknowledged.

This research was sponsored by the Department of Industry, Innovation and Science under the auspices of the AUSMURI program which is a part of the Commonwealth's Next Generation Technologies Fund. A/Prof. Sophie Primig is supported by the UNSW Scientia Fellowship scheme. Asst. Prof. Zibin Chen is supported by the Research Office of The Hong Kong Polytechnic University (Project code: P0039966 & P0039581).

The contributions of Profs. Amy Clarke and Sudarsanam Suresh Babu were funded by the Department of the Navy, Office of Naval Research under ONR award number N00014-18-1-2794. Any opinions, findings, and conclusions or recommendations expressed in this material are those of the author(s) and do not necessarily reflect the views of the Office of Naval Research.

The facilities and technical assistance of the teams at Oak-Ridge National lab are acknowledged for the fabrication of the E-PBF Haynes 282 builds. The research at Oak-Ridge National Laboratory was sponsored by the US Department of Energy, Office of Energy Efficiency and Renewable Energy, Advanced Manufacturing Office under contract DE-AC05-00OR22725 with UT-Battelle, LLC. Access to the Oak Ridge National Laboratory's (ORNL) additive manufacturing equipment at ORNL's Manufacturing Demonstration Facility (MDF) was facilitated by US Department of Energy's Strategic Partnership Projects (SPP) mechanism. More information can be found at https://science.energy.gov/lp/strategic-partnership-projects.

Mr. Alec Saville gratefully acknowledges the National Science Foundation Graduate Research Fellowship, USA, under Grant No. 2019260337 for supporting the analyses related to Fig. 4. Neutron diffraction measurements to generate Fig. 4 were supported by the Los Alamos Neutron Science Center (LANSCE), a NNSA User Facility operated for the US Department of Energy (DOE) by Los Alamos National Laboratory (LANL). LANL is operated by Triad National Security, LLC, for the National Nuclear Security Administration, USA, of US DOE (Contract No. 89233218CNA000001).

Appendix A. Supplementary material

Supplementary data associated with this article can be found in the online version at doi:10.1016/j.addma.2022.103120.

References

[1] L.M. Pike, Long term thermal exposure of HAYNES 282 alloy, in: Proceedings of the 7th Inernational Symposium on Superalloy 718 and Derivatives, The Minerals, Metals & Materials Society, 2010, pp. 645–660.

[2] L.M. Pike, Development of a fabricable gamma-prime (γ′) strengthened superalloy, in: Proceedings of the Superalloys 2008 (Eleventh International Symposium), TMS, 2008, pp. 191–200. ⟨https://doi.org/10.7449/2008/Superalloys_2008_191_200⟩.

[3] P.D. Jablonski, J.A. Hawk, C.J. Cowen, P.J. Maziasz, Processing of advanced cast alloys for A-USC steam turbine applications, JOM 64 (2012) 271–279, https://doi.org/10.1007/s11837-012-0241-4.

[4] P.F. Tortorelli, H. Wang, K.A. Unocic, M.L. Santella, J.P. Shingledecker, V. Cedro, Long-term creep-rupture behavior of Inconel® 740 and Haynes® 282, Am. Soc. Mech. Eng. Digit. Collect. (2017) 29–36, https://doi.org/10.1115/ETAM2014-1003.

[5] R. Viswanathan, J.F. Henry, J. Tanzosh, G. Stanko, J. Shingledecker, B. Vitalis, R. Purgert, U.S. program on materials technology for ultra-supercritical coal power plants, J. Mater. Eng. Perform. 14 (2005) 281–292, https://doi.org/10.1361/10599490524039.

[6] K.L. Kruger, 15 - HAYNES 282 alloy, in: A. Di Gianfrancesco (Ed.), Materials for Ultra-Supercritical and Advanced Ultra-Supercritical Power Plants, Woodhead Publishing, 2017, pp. 511–545, https://doi.org/10.1016/B978-0-08-100552-1.00015-4.

[7] J. Cormier, C.-A. Gandin, Chapter 7 - processing of directionally cast nickel-base superalloys: solidification and heat treatments, in: G. Cailletaud, J. Cormier, G. Eggeler, V. Maurel, L. Nazé (Eds.), Nickel Base Single Crystals Across Length Scales, Elsevier, 2022, pp. 193–222, https://doi.org/10.1016/B978-0-12-819357-0.00015-9.

[8] A. Ramakrishnan, G.P. Dinda, Microstructure and mechanical properties of direct laser metal deposited Haynes 282 superalloy, Mater. Sci. Eng. A 748 (2019) 347–356, https://doi.org/10.1016/j.msea.2019.01.101.

[9] A.S. Shaikh, F. Schulz, K. Minet-Lallemand, E. Hryha, Microstructure and mechanical properties of Haynes 282 superalloy produced by laser powder bed fusion, Mater. Today Commun. 26 (2021), 102038, https://doi.org/10.1016/j.mtcomm.2021.102038.

[10] R. Otto, V. Brøtan, A.S. Azar, O. Åsebø, Processing of Haynes® 282® alloy by laser powder bed fusion technology, in: Proceedings of the TMS 2019 148th Annual Meeting & Exhibition Supplemental Proceedings, Springer International Publishing, Cham, 2019, pp. 503–510. ⟨https://doi.org/10.1007/978-3-030-05861-6_47⟩.

[11] K.A. Unocic, M.M. Kirka, E. Cakmak, D. Greeley, A.O. Okello, S. Dryepondt, Evaluation of additive electron beam melting of haynes 282 alloy, Mater. Sci. Eng. A 772 (2020), 138607, https://doi.org/10.1016/j.msea.2019.138607.

[12] W.J. Sames, F.A. List, S. Pannala, R.R. Dehoff, S.S. Babu, The metallurgy and processing science of metal additive manufacturing, Int. Mater. Rev. 61 (2016) 315–360, https://doi.org/10.1080/09506608.2015.1116649.

[13] A. Takase, T. Ishimoto, R. Suganuma, T. Nakano, Surface residual stress and phase stability in unstable β-type Ti–15Mo–5Zr–3Al alloy manufactured by laser and electron beam powder bed fusion technologies, Addit. Manuf. 47 (2021), 102257, https://doi.org/10.1016/j.addma.2021.102257.

[14] S.S. Babu, N. Raghavan, J. Raplee, S.J. Foster, C. Frederick, M. Haines, R. Dinwiddie, M.K. Kirka, A. Plotkowski, Y. Lee, R.R. Dehoff, Additive manufacturing of nickel superalloys: opportunities for innovation and challenges related to qualification, Metall. Mater. Trans. A 49 (2018) 3764–3780, https://doi.org/10.1007/s11661-018-4702-4.

[15] L.E. Murr, S.M. Gaytan, D.A. Ramirez, E. Martinez, J. Hernandez, K.N. Amato, P. W. Shindo, F.R. Medina, R.B. Wicker, Metal fabrication by additive manufacturing using laser and electron beam melting technologies, J. Mater. Sci. Technol. 28 (2012) 1–14, https://doi.org/10.1016/S1005-0302(12)60016-4.

[16] C. Korner, Additive manufacturing of metallic components by selective electron beam melting - a review, Int. Mater. Rev. 61 (2016) 361–377, https://doi.org/10.1080/09506608.2016.1176289.

[17] T.R. Watkins, K.A. Unocic, A. Peralta, M. Megahed, J.R. Bunn, C.M. Fancher, C. D'Elia, M.R. Hill, J.F. Neumann, Residual stresses and microstructure within Allvac 718Plus laser powder bed fusion bars, Addit. Manuf. (2021), 102334, https://doi.org/10.1016/j.addma.2021.102334.

[18] N. Nadammal, T. Mishurova, T. Fritsch, I. Serrano-Munoz, A. Kromm, C. Haberland, P.D. Portella, G. Bruno, Critical role of scan strategies on the development of microstructure, texture, and residual stresses during laser powder bed fusion additive manufacturing, Addit. Manuf. 38 (2021), 101792, https://doi.org/10.1016/j.addma.2020.101792.

[19] W. Chen, T. Voisin, Y. Zhang, J.-B. Florien, C.M. Spadaccini, D.L. McDowell, T. Zhu, Y.M. Wang, Microscale residual stresses in additively manufactured

stainless steel, Nat. Commun. 10 (2019) 1–12, https://doi.org/10.1038/s41467-019-12265-8.

[20] N. Hrabe, T. Gnäupel-Herold, T. Quinn, Fatigue properties of a titanium alloy (Ti–6Al–4V) fabricated via electron beam melting (EBM): effects of internal defects and residual stress, Int. J. Fatigue 94 (2017) 202–210, https://doi.org/10.1016/j.ijfatigue.2016.04.022.

[21] A. Shaji Karapuzha, D. Fraser, D. Schliephake, S. Dietrich, Y. Zhu, X. Wu, A. Huang, Microstructure, mechanical behaviour and strengthening mechanisms in Hastelloy X manufactured by electron beam and laser beam powder bed fusion, J. Alloy. Compd. 862 (2021), 158034, https://doi.org/10.1016/j.jallcom.2020.158034.

[22] R. Liu, Z. Wang, T. Sparks, F. Liou, J. Newkirk, 13 - Aerospace applications of laser additive manufacturing, in: M. Brandt (Ed.), Laser Additive Manufacturing, Woodhead Publishing, 2017, pp. 351–371, https://doi.org/10.1016/B978-0-08-100433-3.00013-0.

[23] T.D. Ngo, A. Kashani, G. Imbalzano, K.T.Q. Nguyen, D. Hui, Additive manufacturing (3D printing): A review of materials, methods, applications and challenges, Compos. Part B Eng. 143 (2018) 172–196, https://doi.org/10.1016/j.compositesb.2018.02.012.

[24] G.S. Kumar, M. Sateshwar, A.R. Sharma, M. Palit, R. Sarkar, P. Ghosal, G.A. Rao, Particle size dependent microstructure evolution of inert gas atomized nickel base superalloy powders, J. Alloy. Compd. 909 (2022), 164772, https://doi.org/10.1016/j.jallcom.2022.164772.

[25] E. Rodriguez, J. Mireles, C.A. Terrazas, D. Espalin, M.A. Perez, R.B. Wicker, Approximation of absolute surface temperature measurements of powder bed fusion additive manufacturing technology using in situ infrared thermography, Addit. Manuf. 5 (2015) 31–39, https://doi.org/10.1016/j.addma.2014.12.001.

[26] D.B. Williams, C.B. Carter. Transmission Electron Microscopy: A Textbook for Materials Science, second ed., Springer, New York, 2009.

[27] B. Gault, M.P. Moody, J.M. Cairney, S.P. Ringer. Atom Probe Microscopy, Springer Science & Business Media, 2012, https://doi.org/10.1007/978-1-4614-3436-8.

[28] B. Gault, D. Haley, F. de Geuser, M.P. Moody, E.A. Marquis, D.J. Larson, B. P. Geiser, Advances in the reconstruction of atom probe tomography data, Ultramicroscopy 111 (2011) 448–457, https://doi.org/10.1016/j.ultramic.2010.11.016.

[29] S. Takajo, S.C. Vogel, Determination of pole figure coverage for texture measurements with neutron time-of-flight diffractometers, J. Appl. Cryst. 51 (2018) 895–900, https://doi.org/10.1107/S1600576718007732.

[30] L. Lutterotti, S. Matthies, H.-R. Wenk, A.S. Schultz, J.W. Richardson, Combined texture and structure analysis of deformed limestone from time-of-flight neutron diffraction spectra, J. Appl. Phys. 81 (1997) 594–600, https://doi.org/10.1063/1.364220.

[31] A.I. Saville, A. Creuziger, E.B. Mitchell, S.C. Vogel, J.T. Benzing, J. Klemm-Toole, K.D. Clarke, A.J. Clarke, MAUD Rietveld refinement software for neutron diffraction texture studies of single- and dual-phase materials, Integr. Mater. Manuf. Innov. 10 (2021) 461–487, https://doi.org/10.1007/s40192-021-00224-5.

[32] F. Bachmann, R. Hielscher, H. Schaeben, Texture analysis with MTEX – free and open source software toolbox, Solid State Phenom. 160 (2010) 63–68, https://doi.org/10.4028/www.scientific.net/SSP.160.63.

[33] ASTM International, E2546-15 Standard Practice for Instrumented Indentation Testing, ASTM International, West Conshohocken, PA, 2015, https://doi.org/10.1520/E2546-15 accessed September 17, 2020.

[34] W.C. Oliver, G.M. Pharr, An improved technique for determining hardness and elastic modulus using load and displacement sensing indentation experiments, J. Mater. Res. 7 (1992) 1564–1583, https://doi.org/10.1557/JMR.1992.1564.

[35] P.J. Withers, M. Preuss, A. Steuwer, J.W.L. Pang, Methods for obtaining the strain-free lattice parameter when using diffraction to determine residual stress, J. Appl. Cryst. 40 (2007) 891–904, https://doi.org/10.1107/S0021889807030269.

[36] L.M. Sochalski-Kolbus, E.A. Payzant, P.A. Cornwell, T.R. Watkins, S.S. Babu, R. R. Dehoff, M. Lorenz, O. Ovchinnikova, C. Duty, Comparison of residual stresses in Inconel 718 simple parts made by electron beam melting and direct laser metal sintering, Metall. Mater. Trans. A 46 (2015) 1419–1432, https://doi.org/10.1007/s11661-014-2722-2.

[37] D.H. Chung, W.R. Buessem, The Voigt-Reuss-Hill approximation and elastic moduli of polycrystalline MgO, CaF2, β-ZnS, ZnSe, and CdTe, J. Appl. Phys. 38 (1967) 2535–2540, https://doi.org/10.1063/1.1709944.

[38] J.P. Watt, G.F. Davies, R.J. O'Connell, The elastic properties of composite materials, Rev. Geophys. 14 (1976) 541–563, https://doi.org/10.1029/RG014i004p00541.

[39] R.C. Reed, The Superalloys: Fundamentals and Applications, Cambridge University Press, 2008.

[40] F. Prinz, A.S. Argon, W.C. Moffatt, Recovery of dislocation structures in plastically deformed copper and nickel single crystals, Acta Metall. 30 (1982) 821–830, https://doi.org/10.1016/0001-6160(82)90080-3.

[41] F. Theska, S.P. Ringer, S. Primig, Atom probe microscopy of strengthening effects in alloy 718, Microsc. Microanal. 25 (2019) 470–480, https://doi.org/10.1017/S1431927618015611.

[42] F. De Geuser, B. Gault, Metrology of small particles and solute clusters by atom probe tomography, Acta Mater. 188 (2020) 406–415, https://doi.org/10.1016/j.actamat.2020.02.023.

[43] P.J. Withers, H.K.D.H. Bhadeshia, Residual stress. Part 1 – measurement techniques, Mater. Sci. Technol. 17 (2001) 355–365, https://doi.org/10.1179/026708301101509980.

[44] C. Li, Z.Y. Liu, X.Y. Fang, Y.B. Guo, Residual stress in metal additive manufacturing, in: Proceedings of the 4th CIRP Conference on Surface Integrity (CSI 2018), 2018, pp. 348–353. ⟨https://doi.org/10.1016/j.procir.2018.05.039⟩.

[45] P.J. Withers, H.K.D.H. Bhadeshia, Residual stress. Part 2 – nature and origins, Mater. Sci. Technol. 17 (2001) 366–375, https://doi.org/10.1179/026708301101510087.

[46] A.J. Wilkinson, G. Meaden, D.J. Dingley, High-resolution elastic strain measurement from electron backscatter diffraction patterns: new levels of sensitivity, Ultramicroscopy 106 (2006) 307–313, https://doi.org/10.1016/j.ultramic.2005.10.001.

[47] P. Mercelis, J. Kruth, Residual stresses in selective laser sintering and selective laser melting, Rapid Prototyp. J. 12 (2006) 254–265, https://doi.org/10.1108/13552540610707013.

[48] D. Buchbinder, W. Meiners, N. Pirch, K. Wissenbach, J. Schrage, Investigation on reducing distortion by preheating during manufacture of aluminum components using selective laser melting, J. Laser Appl. 26 (2014), 012004, https://doi.org/10.2351/1.4828755.

[49] Sindo Kou. Welding Metallurgy, second ed., John Wiley & Sons, Ltd, Hoboken, New Jersey, 2002 https://doi.org/10.1002/0471434027.

[50] X. Song, S. Feih, W. Zhai, C.-N. Sun, F. Li, R. Maiti, J. Wei, Y. Yang, V. Oancea, L. Romano Brandt, A.M. Korsunsky, Advances in additive manufacturing process simulation: residual stresses and distortion predictions in complex metallic components, Mater. Des. 193 (2020), 108779, https://doi.org/10.1016/j.matdes.2020.108779.

[51] S.I. Shahabad, U. Ali, Z. Zhang, A. Keshavarzkermani, R. Esmaeilizadeh, A. Bonakdar, E. Toyserkani, On the effect of thin-wall thickness on melt pool dimensions in laser powder-bed fusion of Hastelloy X: numerical modeling and experimental validation, J. Manuf. Process. 75 (2022) 435–449, https://doi.org/10.1016/j.jmapro.2022.01.029.

[52] C. Joseph, C. Persson, M. Hörnqvist Colliander, Influence of heat treatment on the microstructure and tensile properties of Ni-base superalloy Haynes 282, Mater. Sci. Eng. A 679 (2017) 520–530, https://doi.org/10.1016/j.msea.2016.10.048.

[53] W.D. Nix, H. Gao, Indentation size effects in crystalline materials: a law for strain gradient plasticity, J. Mech. Phys. Solids 46 (1998) 411–425, https://doi.org/10.1016/S0022-5096(97)00086-0.

[54] P.A.J. Bagot, O.B.W. Silk, J.O. Douglas, S. Pedrazzini, D.J. Crudden, T.L. Martin, M. C. Hardy, M.P. Moody, R.C. Reed, An atom probe tomography study of site preference and partitioning in a nickel-based superalloy, Acta Mater. 125 (2017) 156–165, https://doi.org/10.1016/j.actamat.2016.11.053.

[55] Q. Wu, S. Li, Alloying element additions to Ni3Al: site preferences and effects on elastic properties from first-principles calculations, Comput. Mater. Sci. 53 (2012) 436–443, https://doi.org/10.1016/j.commatsci.2011.09.016.

[56] R. Eriş, M.V. Akdeniz, A.O. Mekhrabov, Atomic size effect of alloying elements on the formation, evolution and strengthening of γ′-Ni3Al precipitates in Ni-based superalloys, Intermetallics 109 (2019) 37–47, https://doi.org/10.1016/j.intermet.2019.02.017.

[57] A.J. Breen, F. Theska, B. Lim, S. Primig, S.P. Ringer, Advanced quantification of the site-occupancy in ordered multi-component intermetallics using atom probe tomography, Intermetallics 145 (2022), 107538, https://doi.org/10.1016/j.intermet.2022.107538.